Epitaxy of Rhodochrosite (MnCO₃) on Muscovite Mica and Its Relation with Calcite (CaCO₃)

Sander J. T. Brugman, Anne B. Ottenbros, Frank Megens, Willem J. P. van Enckevort, and Elias Vlieg*

ACCESS | 📊 Metrics & More | 📄 Article Recommendations | 🆘 Supporting Information

ABSTRACT: The flatness of muscovite mica makes it a convenient substrate to study epitaxy. We have analyzed the growth of rhodochrosite ($MnCO_3$) crystals in solution and on muscovite mica. Growth at high supersaturations occurs via the formation of amorphous $MnCO_3$, which over time transforms into the crystalline form. In the presence of muscovite mica, epitaxial rhodochrosite crystals with a size of approximately 1 μm form. These crystals are kinetically roughened, because of the high supersaturation. The lattice match between $MnCO_3$ and muscovite was found not to be the main reason for epitaxy. If the growth experiment is performed twice, the original epitaxial $MnCO_3$ crystals are overgrown by many small crystallites. Similarly, spherical $MnCO_3$ crystals with many overgrown facets can be formed on a muscovite surface that is exposed to humidity or by using a higher $MnCO_3$ supersaturation. A comparison with calcite shows that epitaxy strongly depends on initial supersaturation for both carbonates. In contrast to previous studies, we find that at the right supersaturation, epitaxial calcite crystal growth is possible on freshly cleaved muscovite.
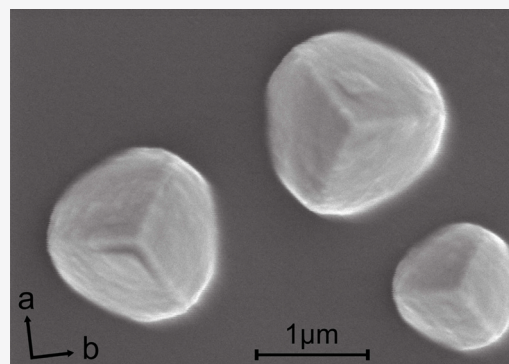
INTRODUCTION

In the past, muscovite mica was used as a cheap alternative to glass in windows in the Moscow area in Russia, as large sheets of the mineral could be obtained, hence the name given to the mineral. Nowadays, in addition to a wide range of industrial applications, muscovite is widely used in scientific experiments. For example, muscovite is used as a model mineral in order to understand enhanced oil recovery,[1,2] to study (hetero)-epitaxy,[3−5] and to create ordered layers of (organic) molecules,[6−8] which in turn can act as a template for protein crystallization.[9,10] A special application for muscovite is found in the surface force apparatus, which is used to measure forces between surfaces.[11] The main reason for using muscovite in these applications is the extreme flatness of the surface obtained after cleavage of the muscovite (001) layers. It is possible to obtain atomically flat areas of over 1 cm² without any steps.[12] Furthermore, the surface properties can be tailored by the exchange of the surface K^+ ions with other cations.[13,14] In the crystal structure of muscovite mica (ideal chemical formula $KAl_2(Si_3Al)O_{10}(OH)_2$), a positive cationic K^+ layer bridges two negatively charged SiO_4 tetrahedral sheets. This layered structure can be easily cleaved through the cationic layer, which was recently suggested to occur at even numbers of layers.[15]

The growth of calcite ($CaCO_3$) on muscovite mica was previously investigated. When grown on freshly cleaved muscovite, calcite crystals have a random orientation.[5] However, when muscovite is first exposed to humid air, small K_2CO_3 nanocrystallites form, which induce epitaxial

growth of the calcite crystals.[5] Here, the growth of carbonates on muscovite (001) is further investigated by looking at the mineral rhodochrosite ($MnCO_3$). Rhodochrosite is isostructural to calcite and is encountered in soil and sediment material, where it plays an important role in the Mn^{2+} geochemistry.[16−18] Furthermore, it has been extensively used as a template material for the formation of hollow-core capsules usable for drug delivery.[19−23] We expect the growth behavior of $MnCO_3$ to be similar to $CaCO_3$. We found, however, that rhodochrosite *does* crystallize epitaxially on freshly cleaved muscovite where calcite was thought not to. This seems conflicting, but we find that at sufficiently large supersaturation epitaxial crystals of calcite can be grown as well.

EXPERIMENTAL METHODS

$MnCO_3$ crystals were grown by adding equal amounts of an aqueous manganese chloride tetrahydrate solution (Sigma-Aldrich, ≥99% pure) to an aqueous sodium carbonate (Fisher Scientific, no indication of purity given) solution. If not stated otherwise, concentrations of 10 mM were used for both solutions, leading to a $MnCO_3$ solution concentration of 5 mM. In the solution growth

experiments, the suspension was filtered after a crystallization time varying from 0 min to several hours, prior to characterization by powder X-ray diffraction and microscopy. In the epitaxy experiments, muscovite mica (ASTM-V1 quality grade, S&J Trading Inc.) was freshly cleaved using Scotch tape. These muscovite samples were adhered to a sample holder by using petroleum jelly and placed upside down in a 24-well plate (ThermoFisher Scientific) filled with the solution. This was then placed in a closed compartment, typically for 2 h. Subsequently, the samples were washed two times in demineralized water for at least 30 s and dried in air. In some of the experiments, pieces of muscovite were, prior to crystallization experiments, exposed to humidity for 1 h in a Binder MKF 115 climate chamber, in which the relative humidity was set at 37.5%. A number of crystal growth experiments was performed twice; i.e., after separation of the specimen from the solution followed by washing and drying, the above procedure is repeated. $CaCO_3$ crystals were grown in a similar way by using a 10 mM calcium chloride solution (Merck, >99.5% pure), or higher concentrations, when indicated. All experiments were performed at room temperature and without any pH adjustments.

The crystallographic orientation of muscovite mica was determined using a Leica DMRX optical polarization microscope in conoscopy mode (see Supporting Information S1 and S2).[9,24] Scanning electron microscopy images were acquired using a PhenomWorld Phenom scanning electron microscope and a JEOL 6330 Cryo field emission scanning electron microscope. For these measurements, a thin gold layer was applied to the samples using a Cressington 108auto sputter coater. As a measure of the epitaxial crystal size, the distance between one corner of the triangular crystal to the middle of the opposite side was used. The crystal sizes of at least two different batches were measured, and for each batch seven random positions were evaluated.

Throughout this article, the hexagonal setting of $MnCO_3$ and $CaCO_3$ is used. The (001) crystal plane in the hexagonal setting corresponds to the (111) plane in the rhombohedral setting, whereas the (104) plane in the hexagonal setting corresponds to the (221) plane in the rhombohedral setting.

The chemical speciation of the solutions and corresponding $MnCO_3$ and $CaCO_3$ saturations were determined using the PHREEQC software.[25] The solution was treated as a closed system with a temperature of 25 °C. Input species were Ca^{2+}/Mn^{2+} (1 equiv), CO_3^{2-} (1 equiv), Na^+ (2 equiv), and Cl^- (2 equiv), where 1 equiv corresponds to the $MnCO_3$ and $CaCO_3$ concentrations mentioned in the text. The saturation index (SI) was calculated by the software according to $SI = \log_{10}(\{A\}^a\{B\}^b/K_{sp})$, with $\{A\}^a$ and $\{B\}^b$ the actual activities of the ions and K_{sp} the solubility product. The driving force of crystallization $(\frac{\Delta\mu}{kT})$ is related to the SI via $\frac{\Delta\mu}{kT} = 2.30\times SI$, with k, the Boltzmann constant and T, the temperature (in K). The calculated values can be found in Table 1.

RESULTS AND DISCUSSION

$MnCO_3$ Growth in Solution. In order to understand the epitaxial growth of $MnCO_3$, we first performed experiments in solution under similar experimental conditions. To obtain $MnCO_3$, solutions containing 10 mM of $MnCl_2$ and 10 mM of Na_2CO_3 were mixed, which immediately leads to the precipitation of white particles in solution. Powder X-ray diffraction (PXRD) measurements performed directly after mixing both compounds showed no crystalline peaks, as is shown in Figure 1a, but an amorphous signal is visible around 18°. We therefore conclude that these particles are amorphous (A-$MnCO_3$). The same conclusion was drawn in a previous study, in which the amorphous phase was found to contain slightly more than one water molecule per $MnCO_3$ moiety.[26]

After a crystallization time of approximately 15 min, peaks start to emerge in the diffractogram. These peaks, corresponding to crystalline $MnCO_3$, i.e., rhodochrosite, become more intense when the crystallization time is increased. Visually, the

Table 1. Calculated Values of pH, Driving Force and Total Concentration of Dissolved Mn^{2+}/Ca^{2+} for Several $MnCO_3$ and $CaCO_3$ Concentrations, Using the PHREEQC Software

concentration (mM)	pH	driving force $(\frac{\Delta\mu}{kT})$	dissolved Ca^{2+}/Mn^{2+} (mM)
		$MnCO_3$	
0.2	9.1	5.2	0.01
0.5	9.1	6.4	0.01
5	9.1	8.9	0.02
25	9.1	10.6	0.02
50	9.2	11.3	0.02
250	9.2	13.0	0.04
		$CaCO_3$	
0.5	9.9	2.8	0.13
1.7	9.9	4.7	0.14
5	9.9	6.1	0.16
25	9.9	8.0	0.21
50	9.9	8.7	0.26
250	9.9	10.5	0.48

transformation from the white amorphous form to the brown crystalline form can be observed as well. After a crystallization time of approximately 25 min, a slight brown color becomes apparent, which agrees with the PXRD measurements. After approximately 2 h, a stable brown color is reached, indicating a considerable amount of crystalline $MnCO_3$. The transformation to crystalline $MnCO_3$ does not stop when the amorphous particles are removed from the solution. After a crystallization time of 5 min in solution, followed by a waiting time of 2 days in air, intense peaks corresponding to rhodochrosite were observed (Figure 1a), whereas without this waiting time no crystals were present.

Figure 1b shows SEM images of $MnCO_3$ crystals obtained after filtration of the solution after a crystallization time of 2 h, followed by a waiting time of 2 days. The smaller crystals of 1—2 μm in size appear rhombohedral. Larger, more spherical particles of about 4—8 μm were also observed. The latter possess many small overgrown facets, as can be seen in Figure 1b. Figure 1c shows a similar crystal of which a part was detached during the filtration process, allowing the observation of the interior of the crystal. The core of the crystal appears hollow. Needle-shaped crystals grow from the inside toward the surface, where they end well-faceted. It is likely that nucleation and growth of the crystallites take place on an amorphous particle, while growth material is supplied by the supersaturated solution. In time, the amorphous particle dissolves, leading to a hollow core. The crystalline phase grows outward by means of evolutionary selection.[27,28] According to Van der Drift's model,[27] the texture of polycrystalline layers on top of a planar or spherical substrate is determined by the fastest growing directions after some period of growth. In the case of $MnCO_3$, this is the [001] top direction and following Van der Drift's evolutionary selection model, the polycrystalline spheres are bound by the [001] apexes of the crystallites pointing outward from the center as shown in Figure 1c.

Epitaxial $MnCO_3$ on Muscovite Mica. *Morphology and Orientation.* Epitaxial growth of $MnCO_3$ was achieved by mixing equimolar 10 mM solutions of Na_2CO_3 and $MnCl_2$ (yielding a 5 mM $MnCO_3$ solution) in the presence of muscovite mica. Scanning electron microscopy images of these epitaxial crystals are shown in Figure 2. Nearly all crystals
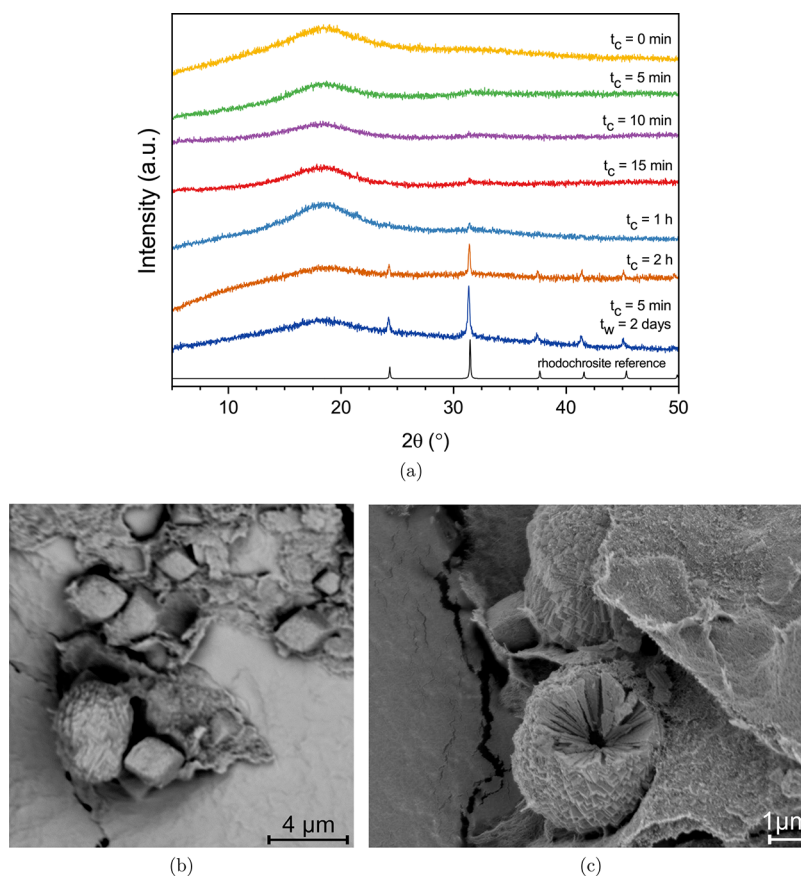
Figure 1. (a) PXRD measurements in which the crystallization time (t_c) is varied. If not mentioned otherwise, the waiting time (t_w) after filtration is kept as short as possible, i.e., several minutes, before the PXRD is conducted. The reference rhodochrosite diffractogram is calculated from the crystal structure.[29] Diffractograms are given a vertical offset for clarity. (b) and (c) SEM images of MnCO$_3$ crystals from a 5 mM solution after a crystallization time of 2 h and a waiting time of 2 days.
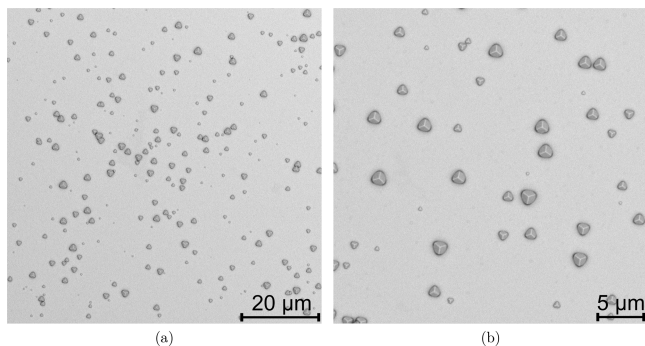

Figure 2. Scanning electron microscopy images of epitaxial MnCO$_3$ crystals on muscovite mica for a 5 mM concentration and after 2 h of crystallization time.

observed are oriented epitaxially (99 ± 1%). The size and density of the crystals are not sufficient to use PXRD to determine the MnCO$_3$ "contact face", i.e., the MnCO$_3$ crystal plane parallel to the muscovite surface. Even an exposure time of more than 100 h did not reveal any detectable MnCO$_3$ reflections, as these are obscured by the mica background X-ray scattering. However, from the 3-fold symmetry and by looking at similarities with epitaxial calcite (CaCO$_3$) on muscovite mica[5] (Supporting Information S2), it can be concluded that the MnCO$_3$ contact face is the (001) plane. Also, careful measurements of the lozenge-shaped faces of several MnCO$_3$ crystals revealed average values of 102.5° for

the obtuse angles and 76.1° for the acute angles. This agrees well with the angle of 103.02° and 76.98° as calculated for the {104} faces of the $R\bar{3}c$ rhodochrosite structure using a = 4.773 Å and c = 15.67 Å in the hexagonal setting. So, the MnCO$_3$ crystallites are bounded by {104} faces, similar to CaCO$_3$. The (pseudo)hexagonal symmetry of the muscovite mica (001) surface, in combination with the 3-fold symmetry of the MnCO$_3$ crystals, gives rise to two distinguishable—opposite— MnCO$_3$ orientations. The detailed measurements of the epitaxial properties of the MnCO$_3$ crystallites on muscovite mica are summarized in the Supporting Information (S3).

Muscovite mica (001) has a rectangular surface unit cell with lattice parameters a = 5.1906 Å and b = 9.0080 Å,[30] which is illustrated in Figure 3a. Figure 3b shows the MnCO$_3$ contact face, i.e., the (001) plane. As this face is polar, two different terminations can be expected: a carbonate termination or a manganese termination. In our case, it is more likely that the Mn^{2+} layer is found directly above mica, as muscovite mica has a negative intrinsic charge caused by isomorphous substitution.[31] The rectangular centered MnCO$_3$ surface unit cell, drawn in Figure 3b, is an alternative for the rhombohedral setting and has lattice parameters a = 4.773 Å and b = 8.267 Å.[29] From the fact that the {104} MnCO$_3$ side facets point toward the muscovite b-axis and its hexagonal equivalents, it follows that both rectangular surface unit cells coincide (see Supporting Information S1 and S3). The Mn^{2+} cations could be located above the center of the muscovite hexagonal cavity, replacing the K$^+$ cations initially present at the muscovite
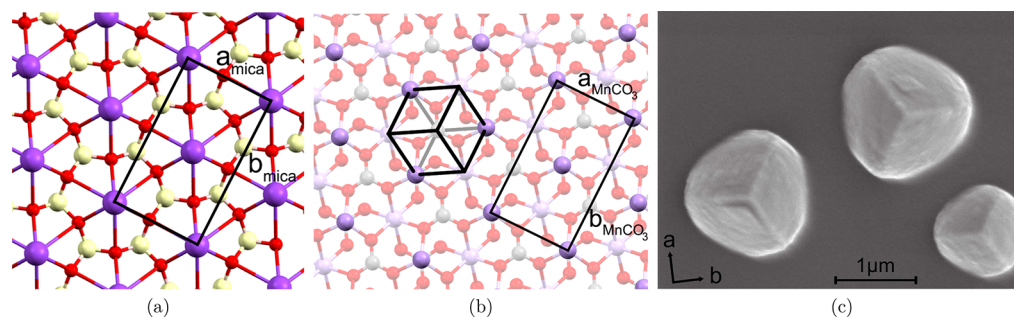
Figure 3. (a) Top view of the muscovite mica crystal structure. The black square indicates the centered unit cell with a = 5.1906 Å and b = 9.0080 Å.[30] (b) The $MnCO_3$ (001) plane. The rhombohedral unit cell displays the 3-fold symmetry observed in the grown crystals. An alternative centered rectangular unit cell with a = 4.773 Å and b = 8.267 Å is drawn as well.[29] The K^+ cations in (a) and Mn^{2+} cations in (b) are shown in purple, O in red, Si in yellow, and C in gray. Panels (a) and (b) are not to the same scale. (c) Scanning electron microscopy images of epitaxial $MnCO_3$ crystals on muscovite mica after 2 h of crystallization time.
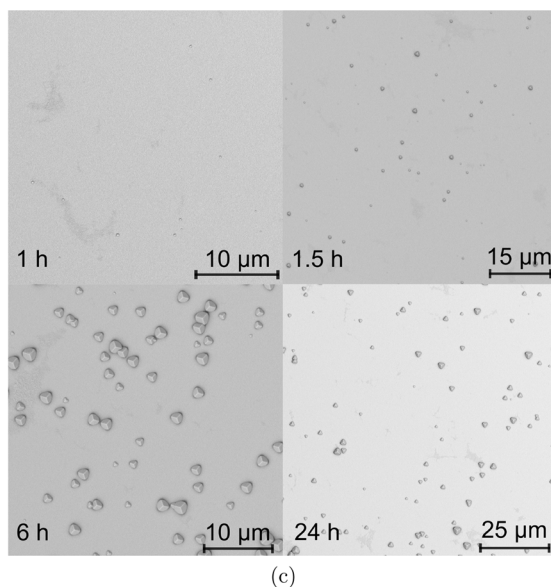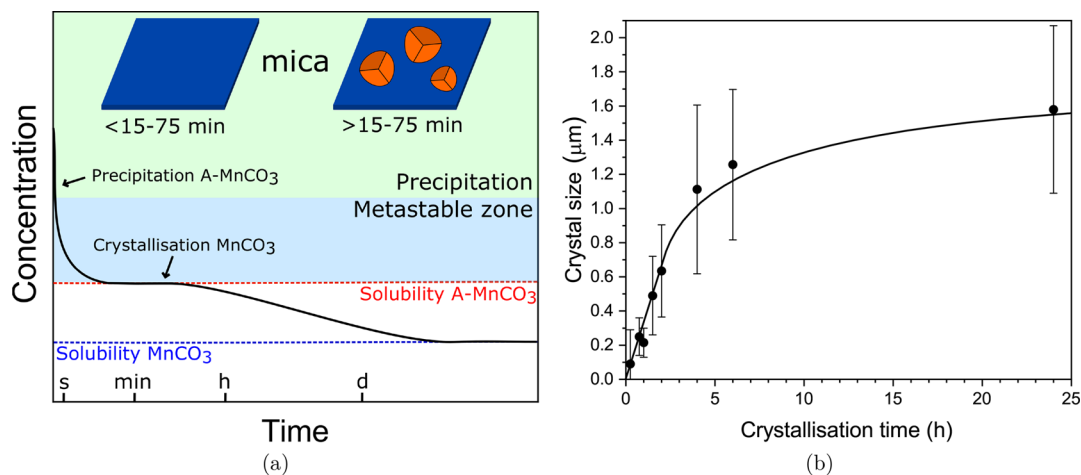

Figure 4. (a) Schematic illustration of the $MnCO_3$ solution concentration as a function of time. After the rapid precipitation of A-$MnCO_3$, the supersaturation is determined by the solubility of A-$MnCO_3$. Then, crystallization takes place, but as long as A-$MnCO_3$ is not yet dissolved, the driving force for crystallization remains constant. When (nearly) all A-$MnCO_3$ is dissolved, the concentraton of $MnCO_3$ decreases until the saturation concentration of $MnCO_3$ is reached and crystallization stops. (b) Average crystal size of epitaxial $MnCO_3$ crystals for the 5 mM initial concentration as a function of time. The solid line is a guide to the eye. Error bars indicate the standard deviation. (c) Selection of SEM images of $MnCO_3$ crystals on muscovite mica at different crystallization times. Note that the figures have different scale bars.

surface. Both the a and b lattice parameters of $MnCO_3$ are 8% smaller than those of muscovite, resulting in an area that is

16% smaller than the area of the muscovite surface unit cell. Remarkably, this lattice mismatch is larger than that of calcite
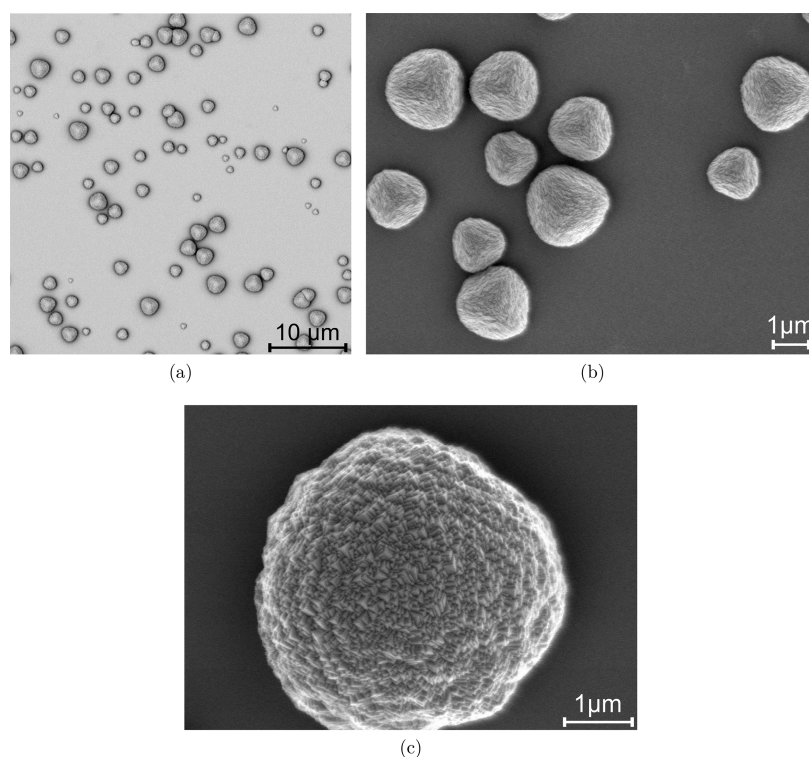
Figure 5. (a−c) Scanning electron microscopy images of epitaxial $MnCO_3$ crystals on muscovite mica after performing two crystal growth cycles of 2 h.

in the same setting (∼4% for both lattice parameters, resulting in an area mismatch of ∼8%).[29] Calcite, which is isostructural to rhodochrosite, is reported not to exhibit epitaxy directly on freshly cleaved muscovite, but epitaxy of calcite can be achieved in the presence of K_2CO_3 nanocrystallites on the muscovite surface.[5] This means that for $MnCO_3$ the lattice match is not the main reason for epitaxy. A similar conclusion was drawn regarding the epitaxy of calcite on muscovite.[5]

Growth. The first epitaxial $MnCO_3$ crystals on the muscovite mica surface are observed after a crystallization time between 15 and 75 min, whereas the amorphous phase in the bulk solution immediately forms when the two solutions are brought together. The solubility of A-$MnCO_3$ is higher than that of crystalline $MnCO_3$,[32] which results in a supersaturated solution with respect to crystalline $MnCO_3$. This leads to sustained growth of crystalline $MnCO_3$ on the mica substrate. This is an example of Ostwald's rule of stages, where first the least stable form is formed, followed by crystallization of the stable form.[33,34] The nucleation barrier for the amorphous phase is lower than that of the crystalline phase. Rapid nucleation of the amorphous phase is followed by slow nucleation and growth of the crystalline phase. If both phases would have a similar nucleation barrier, crystals would form immediately because of the high supersaturation. The evolution is schematically illustrated in Figure 4a, in which the supersaturation is shown as a function of time. When the two solutions are brought together, a large supersaturation is created. This rapidly decreases due to the formation of A-$MnCO_3$ dispersed in solution. After the nucleation of crystalline $MnCO_3$ in solution and at the muscovite surface, A-$MnCO_3$ dissolves leading to a plateau in concentration, followed by a decrease in $MnCO_3$ concentration if A-$MnCO_3$ is completely dissolved, as was earlier observed for $CaCO_3$.[35] This is confirmed by the growth rate measurements displayed in Figure 4b. Initially, the crystals show a linear increase in size over time, as expected for constant supersaturation. Then the growth speed decreases as the solution depletes and approaches the equilibrium concentration of $MnCO_3$. The crystals continue to grow until the equilibrium concentration is reached after approximately 24 h. The epitaxial crystals observed at different crystallization times all possess the same morphology and only differ in size (Figure 4c). At concentrations above approximately 2.5 mM, immediate precipitation of A-$MnCO_3$ occurred, whereas at lower concentrations, no precipitation of A-$MnCO_3$ nor growth of $MnCO_3$ on muscovite was observed. The high supersaturation in this experiment leads to kinetic roughening, resulting in rounded edges of the $MnCO_3$ crystals, as has been seen in Figures 2 and 3c.

In an attempt to increase the size of the crystals, the growth experiment was performed twice. Surprisingly, we observed that the original {104} facets became overgrown, as can be seen in Figure 5. The epitaxy and {104} facets of the $MnCO_3$ crystals are still visible, but many small well-faceted crystallites have grown on top of the original {104} facets. Also in this second crystallization step, because of the high supersaturation, amorphous material precipitates from solution, judging from the white color of the precipitated solid. It is unclear if amorphous particles adhere to the surface of the original $MnCO_3$ crystals and then transform into small $MnCO_3$ crystallites or if they first transform into the crystalline form followed by attachment to the $MnCO_3$ crystals. In both cases, this can lead to the formation of the observed nonepitaxial faceted crystallites on the original crystals. In the second cycle, no nucleation barrier or a very low nucleation barrier for crystallization has to be overcome before growth can occur on top of the existing $MnCO_3$ crystals. This leads to multifaceted growth. However, this is not the case for newly formed crystals
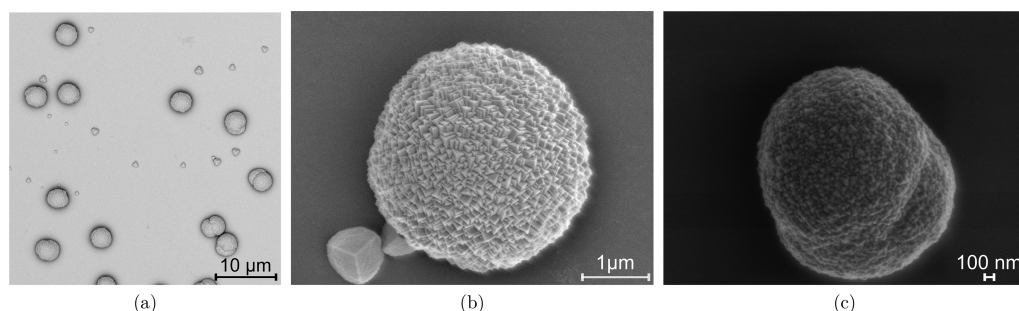
(a)   (b)   (c)

Figure 6. Scanning electron microscopy images of $MnCO_3$ crystals grown on muscovite mica (a) and (b) exposed to humid air followed by 2 h of crystallization time and (c) with a concentration of 25 mM instead of 5 mM on freshly cleaved muscovite mica.

in the second cycle, which are the small crystals observed in Figure 5a.

Epitaxy of calcite on muscovite mica can be achieved by exposing muscovite to humid air prior to the growth experiment.[5] The exposure to humid air is known to lead to epitaxial K_2CO_3 nanocrystals, formed by a combination of muscovite surface K^+ ions and CO_2 from the air.[36,37] Stephens et al. hypothesize that these K_2CO_3 crystallites act as a carbonate source attracting Ca^{2+} to the surface, leading to the epitaxial nucleation of $CaCO_3$ crystals on muscovite mica exposed to humid air.[5] We have also investigated if the presence of K_2CO_3 crystallites on the muscovite surface has an effect on the growth of $MnCO_3$. On the substrates exposed to humid air, still a number of small, epitaxial $MnCO_3$ crystals can be seen, but in contrast to freshly cleaved mica, also larger, nearly spherical $MnCO_3$ crystals are formed (Figure 6a,b). In contrast to the crystals grown by performing two crystal growth cycles on bare muscovite (Figure 5), the larger crystals grown on muscovite exposed to humid air do not have underlying {104} facets of the epitaxial $MnCO_3$ crystals and therefore are nearly spherical. It is likely that the smaller crystals nucleate on the bare muscovite surface and will form epitaxial $MnCO_3$ crystals similar to those on a freshly cleaved muscovite surface, whereas when nucleation takes place on top of the K_2CO_3 crystallites existing on the muscovite mica exposed to humid air, large spherical crystals form.

$MnCO_3$ crystals grown at higher supersaturations on freshly cleaved muscovite, often while stirring the solution, show a similar shape as the multifaceted spherical crystals. The high supersaturation can be achieved by using a high concentration (Figure 6c) or by adding solvents in which $MnCO_3$ is less soluble.[19,23,38,39] In Figure 6c, a concentration of 25 mM is used, which leads to formation of exclusively spherical $MnCO_3$ crystals and no epitaxial crystals. At these higher supersaturations, nucleation can take place at the bare muscovite or on amorphous particles adsorbed at the muscovite surface, similar to crystallization in solution (Figure 1b,c). In both cases, the high supersaturation leads to fast and evolutionary growth which results in the multifaceted crystals.

Comparison with Calcite. Given the different observed behavior in epitaxial growth between $MnCO_3$ (our results) and $CaCO_3$,[5] we now take a detailed looked at these two systems. Earlier we saw that the lattice mismatch is not the main cause of epitaxy for these carbonates. When comparing $MnCO_3$ and $CaCO_3$, many physical parameters are similar. Both Mn^{2+} and Ca^{2+} adsorb at the muscovite surface with similar occupancies.[14] Also, the hydration energy of Mn^{2+} and Ca^{2+} is comparable.[40] The ionic radius of Mn^{2+} is somewhat smaller than that of Ca^{2+} (0.83 and 1.0 Å respectively).[41] It is known

that cations adsorb at different heights at the muscovite interface, depending on hydration energy, valency, and size,[42−46] but the differences in these parameters are small in this case. The solubility, on the other hand, shows a large difference. The solubility product of rhodochrosite is approximately a factor 200 lower than that of calcite.[47,48] As presented above, in some of our experiments the solution concentration is determined by the presence of amorphous material. A rough estimate of the solubility of A-$MnCO_3$ is 0.2 mM, which was determined by diluting A-$MnCO_3$ suspensions until a clear solution was obtained. This is approximately a factor eight lower than for amorphous $CaCO_3$ (1.7 mM).[49] On the basis of the above, the initial supersaturation of $MnCO_3$ and $CaCO_3$ for a 5 mM solution is $\frac{\Delta\mu}{kT} = 8.9$ and $\frac{\Delta\mu}{kT} = 6.1$, respectively (Table 1). The supersaturation during growth in the presence of the amorphous phase is $\frac{\Delta\mu}{kT} = 5.2$ for $MnCO_3$ and $\frac{\Delta\mu}{kT} = 4.7$ for $CaCO_3$. The experiments that result in epitaxial $MnCO_3$ are thus performed at a much higher initial supersaturation than used in the experiments on $CaCO_3$ growth reported earlier. To test if similar high (super)-saturations for $CaCO_3$ would yield epitaxial calcite crystals on freshly cleaved muscovite, we performed experiments using a concentration of 50 mM. This gives a driving force ($\frac{\Delta\mu}{kT} = 8.7$) that is similar to that of a 5 mM $MnCO_3$ solution ($\frac{\Delta\mu}{kT} = 8.9$). Using this $CaCO_3$ concentration of 50 mM, epitaxy of $CaCO_3$ was indeed achieved, as is shown in Figure 7a. The number of epitaxial $CaCO_3$ crystals is smaller than when grown on muscovite exposed to humidity.[5] Moreover, most of these crystals are overgrown.
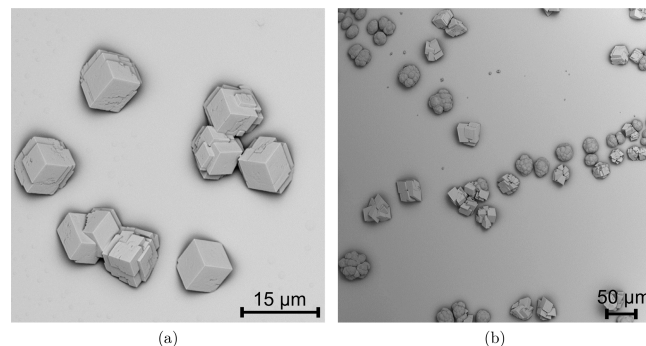

(a)   (b)

Figure 7. Scanning electron microscopy images of $CaCO_3$ crystals grown on muscovite mica after 2 h of crystallization time at a concentration of (a) 50 mM and (b) 250 mM.

As the amorphous phase precipitates, the concentration will rapidly reach the solubility of the amorphous phase. After this time, the supersaturation is expected to be the same as for a concentration of 5 mM, only a larger amount of material precipitates. For 5 mM $CaCO_3$ solutions, no epitaxial calcite is formed on freshly cleaved muscovite, while such growth occurs for 50 mM solutions. Since both concentrations are above the solubility of amorphous $CaCO_3$, we conclude that the high initial concentration is important and that the nuclei for epitaxial $CaCO_3$ are likely already formed in the initial phase. The high supersaturation may result in sufficiently large areas with a high local Ca^{2+} concentration in the geometry as sketched in Figure 3b that lead to nucleation. Further growth of the oriented nuclei leads to the observed epitaxial crystals. The same mechanism likely occurs occurs for $MnCO_3$. While in both cases the supersaturation is similar, for $MnCO_3$ the equilibrium concentration is much lower. This implies a higher surface free energy,[50] resulting in a higher activation barrier for secondary 3D nucleation, which leads to epitaxial crystals without the overgrowth (2), in contrast to $CaCO_3$, where we do see this overgrowth (Figure 7a).

At a concentration of 250 mM and higher, all calcite crystals are overgrown, as can be seen in Figure 7b. Because of the overgrowth, it is unclear if the underlying crystals are epitaxial with the muscovite substrate. The calcite crystals differ in morphology from the spherical overgrown $MnCO_3$ crystals in Figure 6c, but both form at high concentrations. Besides the overgrown calcite crystals, also vaterite crystals are formed (Supporting Information S4). Vaterite is known to be an intermediate phase for the formation of calcite.[51,52]

When the growth experiment is performed twice with 5 mM $CaCO_3$, the calcite crystals continued to grow in a regular fashion, in contrast to $MnCO_3$ (Figure 5), as can be clearly seen from the persistence of the planar {104} facets (Supporting Information S5). Even when the two growth cycles with $CaCO_3$ are performed with a 50 mM concentration (for both cycles) no differences in morphology are observed compared to the 5 mM case (Supporting Information S5). This again shows the effect of the solubility and thus supersaturation of both carbonates on the crystal growth and morphology.

CONCLUSION

We have demonstrated the epitaxial growth of $MnCO_3$ crystals on the muscovite surface. These epitaxial crystals are kinetically roughened because of the high supersaturation. By repeating the crystallization procedure, many small crystals grow on the pre-existing epitaxial $MnCO_3$ crystals, of which the underlying epitaxy remains visible. The formation of large spherical polycrystalline $MnCO_3$ crystals is induced by the presence of K_2CO_3 crystallites formed by exposure of muscovite mica to a humid environment. Similar results can be achieved by using a higher $MnCO_3$ supersaturation. Also epitaxy of $CaCO_3$ on freshly cleaved muscovite was achieved by performing experiments at a similar supersaturation as that of $MnCO_3$, showing that the initial supersaturation and not lattice match is the major parameter in achieving epitaxy.

ASSOCIATED CONTENT

ⓈⒾ Supporting Information

The Supporting Information is available free of charge at https://pubs.acs.org/doi/10.1021/acs.cgd.0c00578.

Conoscopy of $MnCO_3$ and $CaCO_3$ crystals, determination of epitaxial orientation of $MnCO_3$ crystals, and additional SEM images (PDF)

AUTHOR INFORMATION

Corresponding Author
Elias Vlieg − *Institute for Molecules and Materials, Radboud University, 6525AJ Nijmegen, The Netherlands;* ⓞ orcid.org/ 0000-0002-1343-4102; Email: e.vlieg@science.ru.nl

Authors
Sander J. T. Brugman − *Institute for Molecules and Materials, Radboud University, 6525AJ Nijmegen, The Netherlands*
Anne B. Ottenbros − *Institute for Molecules and Materials, Radboud University, 6525AJ Nijmegen, The Netherlands*
Frank Megens − *Institute for Molecules and Materials, Radboud University, 6525AJ Nijmegen, The Netherlands*
Willem J. P. van Enckevort − *Institute for Molecules and Materials, Radboud University, 6525AJ Nijmegen, The Netherlands;* ⓞ orcid.org/0000-0001-7436-8391

Complete contact information is available at:
https://pubs.acs.org/10.1021/acs.cgd.0c00578

Notes
The authors declare no competing financial interest.

REFERENCES

(1) Liu, L.; Buckley, J. S. Alteration of wetting of mica surfaces. *J. Pet. Sci. Eng.* **1999**, *24*, 75−83.

(2) Haagh, M. E. J.; Siretanu, I.; Duits, M. H. G.; Mugele, F. Salinity-dependent contact angle alteration in oil/brine/silicate systems: the critical role of divalent cations. *Langmuir* **2017**, *33*, 3349−3357.

(3) Royer, L. Recherches expérimentales sur l'épitaxie ou orientation mutuelle de cristaux d'espèces différentes. *Bull. Soc. Fr. Mineral.* **1928**, *51*, 7−154.

(4) Ueno, K.; Saiki, K.; Shimada, T.; Koma, A. Epitaxial growth of transition metal dichalcogenides on cleaved faces of mica. *J. Vac. Sci. Technol., A* **1990**, *8*, 68−72.

(5) Stephens, C. J.; Mouhamad, Y.; Meldrum, F. C.; Christenson, H. K. Epitaxy of calcite on mica. *Cryst. Growth Des.* **2010**, *10*, 734−738.

(6) van den Bruele, F. J.; De Poel, W.; Sturmans, H. W. M.; Pintea, S.; de Gelder, R.; Wermeille, D.; Juríček, M.; Rowan, A. E.; van Enckevort, W. J. P.; Vlieg, E. Monolayer and aggregate formation of a modified phthalocyanine on mica determined by a delicate balance of surface interactions. *Surf. Sci.* **2012**, *606*, 830−835.

(7) de Poel, W.; Pintea, S.; de Jong, A.; Drnec, J.; Carlà, F.; Felici, R.; op den Camp, H.; Elemans, J. A. A. W.; van Enckevort, W. J. P.; Rowan, A. E.; Vlieg, E. Dibenzo crown ether layer formation on muscovite mica. *Langmuir* **2014**, *30*, 12570−12577.

(8) de Poel, W.; Brugman, S. J. T.; Ven, K. H. A.; Gasseling, A.; Lange, J.; Townsend, E. R.; Engwerda, A. H. J.; Jankowski, M.; Blijlevens, M. A. R.; Werkhoven, B. L.; Drnec, J.; Carla, F.; Felici, R.; Tuladhar, A.; Adhikari, N. M.; De Yoreo, J. J.; Elemans, J. A. A. W.; Enckevort, W. J. P.; Rowan, A. E.; Vlieg, E. Organothiol Monolayer

Formation Directly on Muscovite Mica. *Angew. Chem.* **2020**, *132*, 2343−2347.

(9) de Poel, W.; Münninghoff, J. A. W.; Elemans, J. A. A. W.; Van Enckevort, W. J. P.; Rowan, A. E.; Vlieg, E. Surfaces with Controllable Topography and Chemistry Used as a Template for Protein Crystallization. *Cryst. Growth Des.* **2018**, *18*, 763−769.

(10) de Poel, W.; Elemans, J. A. A. W.; van Enckevort, W. J. P.; Rowan, A. E.; Vlieg, E. Epitaxial Crystallization of Insulin on an Ordered 2D Polymer Template. *Chem. - Eur. J.* **2019**, *25*, 3756−3760.

(11) Israelachvili, J.; Min, Y.; Akbulut, M.; Alig, A.; Carver, G.; Greene, W.; Kristiansen, K.; Meyer, E.; Pesika, N.; Rosenberg, K.; Zeng, H. Recent advances in the surface forces apparatus (SFA) technique. *Rep. Prog. Phys.* **2010**, *73*, 036601.

(12) de Poel, W.; Pintea, S.; Drnec, J.; Carlà, F.; Felici, R.; Mulder, P.; Elemans, J. A. A. W.; van Enckevort, W. J. P.; Rowan, A. E.; Vlieg, E. Muscovite mica: Flatter than a pancake. *Surf. Sci.* **2014**, *619*, 19−24.

(13) Gaines, G., Jr. The ion-exchange properties of muscovite mica. *J. Phys. Chem.* **1957**, *61*, 1408−1413.

(14) de Poel, W.; Vaessen, S. L.; Drnec, J.; Engwerda, A. H. J.; Townsend, E. R.; Pintea, S.; de Jong, A. E. F.; Jankowski, M.; Carlà, F.; Felici, R.; Elemans, J. A. A. W.; van Enckevort, W. J. P.; Rowan, A. E.; Vlieg, E. Metal ion-exchange on the muscovite mica surface. *Surf. Sci.* **2017**, *665*, 56−61.

(15) Tuladhar, A.; Chase, Z. A.; Baer, M. D.; Legg, B. A.; Tao, J.; Zhang, S.; Winkelman, A. D.; Wang, Z.; Mundy, C.; De Yoreo, J. J.; Wang, H.-f. Direct Observation of the Orientational Anisotropy of Buried Hydroxyl Groups Inside Muscovite Mica. *J. Am. Chem. Soc.* **2019**.*1412135*

(16) Suess, E. Mineral phases formed in anoxic sediments by microbial decomposition of organic matter. *Geochim. Cosmochim. Acta* **1979**, *43*, 339−352.

(17) Pedersen, T. F.; Price, N. B. The geochemistry of manganese carbonate in Panama Basin sediments. *Geochim. Cosmochim. Acta* **1982**, *46*, 59−68.

(18) Bourg, A. C. M.; Bertin, C. Seasonal and spatial trends in manganese solubility in an alluvial aquifer. *Environ. Sci. Technol.* **1994**, *28*, 868−876.

(19) Antipov, A. A.; Shchukin, D.; Fedutik, Y.; Petrov, A. I.; Sukhorukov, G. B.; Möhwald, H. Carbonate microparticles for hollow polyelectrolyte capsules fabrication. *Colloids Surf., A* **2003**, *224*, 175−183.

(20) Zhu, H.; Stein, E. W.; Lu, Z.; Lvov, Y. M.; McShane, M. J. Synthesis of size-controlled monodisperse manganese carbonate microparticles as templates for uniform polyelectrolyte microcapsule formation. *Chem. Mater.* **2005**, *17*, 2323−2328.

(21) Tong, W.; Gao, C. Selective removal of particle cores to fabricate manganese carbonate hollow spheres and composite microcapsules. *Colloids Surf., A* **2007**, *295*, 233−238.

(22) Wei, Q.; Ai, H.; Gu, Z. Matrix polyelectrolyte capsules based on polysaccharide/MnCO3 hybrid microparticle templates. *Colloids Surf., B* **2011**, *85*, 63−72.

(23) Lee, H.-K.; Sakemi, D.; Selyanchyn, R.; Lee, C.-G.; Lee, S.-W. Titania Nanocoating on MnCO3Microspheres via Liquid-Phase Deposition for Fabrication of Template-Assisted Core−Shell-and Hollow-Structured Composites. *ACS Appl. Mater. Interfaces* **2014**, *6*, 57−64.

(24) Wahlstrom, E. E. *Optical Crystallography*; John Wiley & Sons, 1979.

(25) Parkhurst, D. L.; Appelo, C. A. J. Description of input and examples for PHREEQC version 3: a computer program for speciation, batch-reaction, one-dimensional transport, and inverse geochemical calculations. *U.S. Geological Survey* **2013**. DOI: 10.3133/tm6A43

(26) Radha, A. V.; Navrotsky, A. Manganese carbonate formation from amorphous and nanocrystalline precursors: Thermodynamics and geochemical relevance. *Am. Mineral.* **2014**, *99*, 1063−1070.

(27) Van der Drift, A. Evolutionary selection, a principle governing growth orientation in vapour-deposited layers. *Philips Res. Rep.* **1967**, *22*, 267.

(28) Schermer, J. J.; de Theije, F. K.; Elst, W. A. L. M. On the mechanism of< 0 0 1> texturing during flame deposition of diamond. *J. Cryst. Growth* **2002**, *243*, 302−318.

(29) Maslen, E.; Streltsov, V.; Streltsova, N.; Ishizawa, N. Electron density and optical anisotropy in rhombohedral carbonates. III. Synchrotron X-ray studies of CaCO3, MgCO3 and MnCO3. *Acta Crystallogr., Sect. B: Struct. Sci.* **1995**, *51*, 929−939.

(30) Güven, N. The crystal structures of 2 M1 phengite and 2 M1 muscovite. *Z. Kristallogr. - Cryst. Mater.* **1971**, *134*, 196−212.

(31) Bragg, W. L. *Atomic Structure of Minerals*; Cornell University Press, 1937.

(32) Leukel, S.; Tremel, W. Water-Controlled Crystallization of CaCO3, SrCO3, and MnCO3 from Amorphous Precursors. *Cryst. Growth Des.* **2018**, *18*, 4662−4670.

(33) Ostwald, W. Studien über die Bildung und Umwandlung fester Körper. *Z. Phys. Chem.* **1897**, *22U*, 289−330.

(34) De Yoreo, J. J.; Vekilov, P. G. Principles of crystal nucleation and growth. *Rev. Mineral. Geochem.* **2003**, *54*, 57−93.

(35) Clarkson, J. R.; Price, T. J.; Adams, C. J. Role of metastable phases in the spontaneous precipitation of calcium carbonate. *J. Chem. Soc., Faraday Trans.* **1992**, *88*, 243−249.

(36) Christenson, H. K.; Israelachvili, J. N. Growth of ionic crystallites on exposed surfaces. *J. Colloid Interface Sci.* **1987**, *117*, 576−577.

(37) Ostendorf, F.; Schmitz, C.; Hirth, S.; Kühnle, A.; Kolodziej, J. J.; Reichling, M. Evidence for potassium carbonate crystallites on air-cleaved mica surfaces. *Langmuir* **2009**, *25*, 10764−10767.

(38) Fei, J. B.; Cui, Y.; Yan, X. H.; Qi, W.; Yang, Y.; Wang, K.; He, Q.; Li, J. B. Controlled preparation of MnO2 hierarchical hollow nanostructures and their application in water treatment. *Adv. Mater.* **2008**, *20*, 452−456.

(39) Xiao, L.; Wang, S.; Wang, Y.; Meng, W.; Deng, B.; Qu, D.; Xie, Z.; Liu, J. High-capacity and self-stabilized manganese carbonate microspheres as anode material for lithium-ion batteries. *ACS Appl. Mater. Interfaces* **2016**, *8*, 25369−25378.

(40) Marcus, Y. A simple empirical model describing the thermodynamics of hydration of ions of widely varying charges, sizes, and shapes. *Biophys. Chem.* **1994**, *51*, 111−127.

(41) Shannon, R. D. Revised effective ionic radii and systematic studies of interatomic distances in halides and chalcogenides. *Acta Crystallogr., Sect. A: Cryst. Phys., Diffr., Theor. Gen. Crystallogr.* **1976**, *32*, 751−767.

(42) Lee, S. S.; Fenter, P.; Nagy, K. L.; Sturchio, N. C. Monovalent ion adsorption at the muscovite (001)−solution interface: Relationships among ion coverage and speciation, interfacial water structure, and substrate relaxation. *Langmuir* **2012**, *28*, 8637−8650.

(43) Pintea, S.; de Poel, W.; de Jong, A. E. F.; Vonk, V.; van der Asdonk, P.; Drnec, J.; Balmes, O.; Isern, H.; Dufrane, T.; Felici, R.; Vlieg, E. Solid-Liquid Interface Structure of Muscovite Mica in CsCl and RbBr Solutions. *Langmuir* **2016**, *32*, 12955−12965.

(44) Pintea, S.; de Poel, W.; de Jong, A. E. F.; Felici, R.; Vlieg, E. Solid-Liquid Interface Structure of Muscovite Mica in SrCl2 and BaCl2 Solutions. *Langmuir* **2018**, *34*, 4241−4248.

(45) Brugman, S. J. T.; Townsend, E. R.; Smets, M. M. H.; Accordini, P.; Vlieg, E. Concentration-Dependent Adsorption of CsI at the Muscovite−Electrolyte Interface. *Langmuir* **2018**, *34*, 3821−3826.

(46) Brugman, S. J. T.; Werkhoven, B. L.; Townsend, E. R.; Accordini, P.; van Roij, R.; Vlieg, E. Monovalent − divalent cation competition at the muscovite mica surface: Experiment and theory. *J. Colloid Interface Sci.* **2020**, *559*, 291−303.

(47) Johnson, K. S. Solubility of rhodochrosite (MnCO3) in water and seawater. *Geochim. Cosmochim. Acta* **1982**, *46*, 1805−1809.

(48) Plummer, L. N.; Busenberg, E. The solubilities of calcite, aragonite and vaterite in CO2-H2O solutions between 0 and 90 C, and

an evaluation of the aqueous model for the system $CaCO_3$-CO_2-H_2O. *Geochim. Cosmochim. Acta* **1982**, *46*, 1011−1040.

(49) Brečević, L.; Nielsen, A. E. Solubility of amorphous calcium carbonate. *J. Cryst. Growth* **1989**, *98*, 504−510.

(50) Söhnel, O. Electrolyte crystal-aqueous solution interfacial tensions from crystallization data. *J. Cryst. Growth* **1982**, *57*, 101−108.

(51) Rodriguez-Blanco, J. D.; Shaw, S.; Benning, L. G. The kinetics and mechanisms of amorphous calcium carbonate (ACC) crystallization to calcite, via vaterite. *Nanoscale* **2011**, *3*, 265−271.

(52) Bots, P.; Benning, L. G.; Rodriguez-Blanco, J.-D.; Roncal-Herrero, T.; Shaw, S. Mechanistic insights into the crystallization of amorphous calcium carbonate (ACC). *Cryst. Growth Des.* **2012**, *12*, 3806−3814.